
Physically-primed deep-neural-networks for generalized undersampled MRI reconstruction

Nitzan Avidan

Faculty of Biomedical Engineering,
Technion - Israel Institute of Technology
Israel
nitzan.avidan@campus.technion.ac.il

Moti Freiman

Faculty of Biomedical Engineering,
Technion - Israel Institute of Technology
Israel
moti.freiman@technion.ac.il

Abstract

A plethora of deep-neural-networks (DNN) based methods were proposed over the past few years to address the challenging ill-posed inverse problem of MRI reconstruction from undersampled “k-space” (Fourier domain) data. However, instability against variations in the acquisition process and the anatomical distribution, indicates a poor generalization of the relevant physical models by the DNN architectures compared to their classical counterparts. The poor generalization effectively precludes DNN applicability for undersampled MRI reconstruction in the clinical setting. We improve the generalization capacity of DNN methods for undersampled MRI reconstruction by introducing a physically-primed DNN architecture and training approach. Our architecture encodes the undersampling mask in addition to the observed data in the model architecture and employs an appropriate training approach that uses data generated with various undersampling masks to encourage the model to generalize the undersampled MRI reconstruction problem. We demonstrated the added-value of our approach through extensive experimentation with the publicly available Fast-MRI dataset. Our physically-primed approach achieved an enhanced generalization capacity which resulted in significantly improved robustness against variations in the acquisition process and in the anatomical distribution, especially in pathological regions, compared to both vanilla DNN methods and DNN trained with undersampling mask augmentation. Trained models and code to replicate our experiments will become available for research purposes upon acceptance.

1 Introduction

Magnetic resonance imaging (MRI) is a non-invasive imaging modality with a wide range of clinical applications due to its capacity to provide detailed soft-tissue images. The MRI signal is acquired in the Fourier space, called the “k-space”. An inverse Fourier transform (IFT) of the k-space is then applied to generate a meaningful MRI scan in the spatial domain [1]. Acquisition times required to sample the full k-space are a major limiting factor for achieving high spatial and temporal resolutions, reduce motion artifacts, improve patient experience and reduce costs [2].

Partial sampling of the k-space can linearly reduce acquisition times. However, the reconstruction of an MRI image from undersampled k-space data results in a highly ill-posed inverse problem. Naïve reconstruction by zero-filling of the missing k-space data and application of the IFT results in a clinically meaningless image due to the presence of various artifacts [2]. Early works concentrated on the properties of the k-space, such as partial Fourier imaging methods that utilize Hermitian symmetry to reduce acquisition times [3].

Classical linear approaches for MRI reconstruction from undersampled data leverage advances in parallel imaging using multiple receiver coils coupled with linear algorithms for reconstruction

applied either in the k-space domain [4] or in the spatial domain [5]. Nevertheless, the theoretical acceleration factor is bounded by the number of available coils [6]. The practical acceleration factor is further limited due to noise amplification resulted from the matrix inversion [5].

The non-linear compressed sensing (CS) [7] approach aims to reconstruct a high-quality image from undersampled k-space data by constraining the associated ill-posed inverse problem with a sparsity prior by means of a sparsifying linear transform. While the CS objective function does not have a closed form solution, it is a convex problem, and thus, can be solved using numerous iterative algorithms [6].

During the past few years, a plethora of deep-neural-networks (DNN) based methods were proposed for undersampled MRI reconstruction with substantial gains in both image quality and acceleration factors [8]. Similar to the classical methods, DNN-based methods can be applied in both the spatial domain and in the k-space domain. The KIKI-net, for example, alternates between the image domain (I-CNN) and k-space (K-CNN) iteratively, where a data consistency constraint is enforced in an interleaving manner [9]. The more recent End-to-End Variational Network (E2E-VarNet) simultaneously estimates coil-specific sensitivity maps and predicts the fully-sampled k-space from the undersampled k-space data through a series of cascades [10].

Despite the promising performance of currently available DNN methods, Antun et al. [11] and Jalal et al. [12] demonstrated that, unlike their classical counterparts, DNN-based methods are unstable against the presence of variations in the acquisition process and the anatomical distribution. Examples of such variations include using different undersampling mask or acceleration factor during inference compared to those used during training, and the presence of small pathologies or different anatomies compared to the data used for training.

Preliminary works aimed to address the stability gap in DNN-based MRI reconstruction through data augmentation techniques. Specifically, Liu et al. improves overall reconstruction performance and robustness against sampling pattern discrepancies and images acquired at different contrast phases by augmenting the undersampled data with extensively varying undersampling patterns [13]. More recently, Jalal et al. [12] combined DNN-based generative prior with classical CS-based reconstruction and posterior sampling to overcome the stability gap. However, this approach does not directly address the stability gap in DNN-based MRI reconstruction methods.

More recently, physics-driven deep learning methods have emerged as a powerful tool to improve DNN-based undersampled MRI reconstruction generalization capacity. Spanning methods that incorporate physics of MRI acquisitions by means of physics-driven loss functions, plug-and-play methods, generative models, and unrolled networks [6]. Specific examples include enforcing k-space consistency directly after image enhancement [14], and adding k-space consistency as an additional cost function term during training [15].

Yet, the stability of DNN-based methods against variations in the acquisition process and the anatomical distribution remains an open question [6]. Further, current DNN methods formulate the ill-posed undersampled MRI reconstruction problem as a regression task, in which the goal is to predict the fully-sampled k-space data or high quality image from the undersampled data, effectively eliminating the sampling mask used during acquisition, from the regression process at inference time. This is in contrast to their classical counterparts which encode the sampling mask as part of the forward model of the system during the optimization process.

In this work, we aim to address the stability gap in undersampled MRI reconstruction with DNN by introducing a physically-primed DNN architecture and training approach. Unlike previous approaches, our architecture encodes the undersampling mask in addition to the observed data in the model architecture, and employs an appropriate training approach that uses data generated with various undersampling masks to encourage the model to generalize the undersampled MRI reconstruction problem.

Our specific contributions are: 1) the introduction of the physically-primed approach for DNN-based MRI reconstruction from undersampled “k-space” data, 2) improved generalization capacity and robustness against variations in the acquisition process and the anatomical distribution, and; 3) experimental evidence for improved robustness, especially in clinically relevant regions, using the publicly available fastMRI dataset. Fig. 1 concisely depicts our main result. The improved generalization capacity and robustness against variations in the acquisition process (i.e. differences in

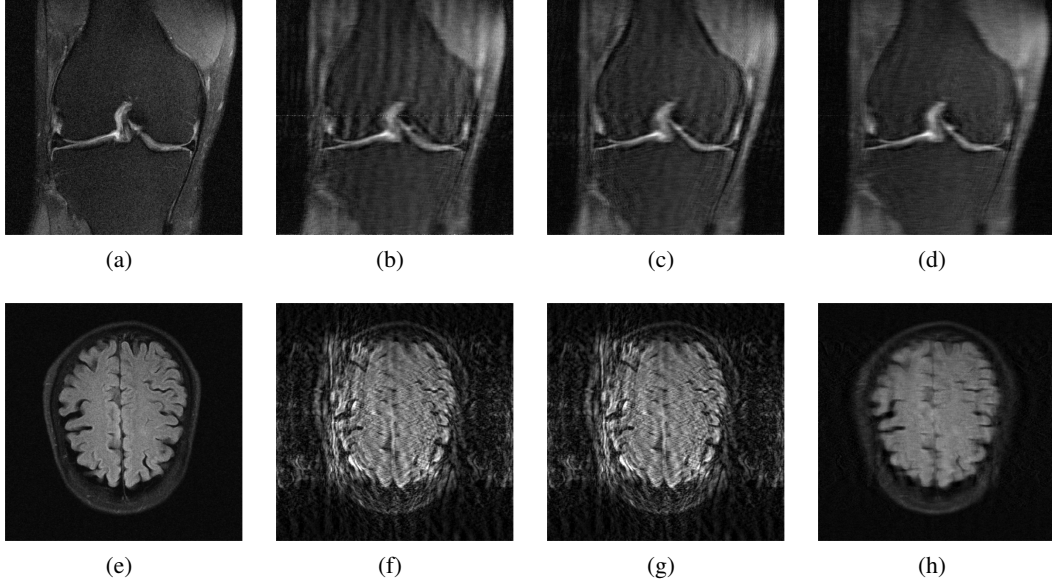


Figure 1: The stability gap in DNN-based MRI reconstruction from undersampled data. First row depicts variation in the acquisition process (different undersampling mask) while the second row presents variation in the anatomical distribution (train on knee data and inference on brain data). (a/e) The target image from fully-sampled k-space data, (b/f) reconstruction using a model trained with a fixed sampling mask (PSNR=24.9/14.07, SSIM=0.4684/0.1926), (c/g) reconstruction using a model trained with mask augmentations (PSNR=25.35/16.56, SSIM=0.4969/0.2812), and; (d/h) reconstruction using the proposed physically-primed approach (PSNR=26.4/26.05, SSIM=0.5354/0.6359).

the undersampling masks) of our physically-primed approach (d,h) compared to baseline methods (b,f, and c,g).

Trained models and code to replicate our experiments will become available for research purposes upon acceptance.

2 Background

The forward model of the undersampled single coil MRI acquisition process is given by:

$$k_{us} = M \circ \mathcal{F}x + n \quad (1)$$

where $k_{us} \in \mathbb{C}^N$ are the observed measurements in the k-space, $x \in \mathbb{R}^N$ is the image representing the underlying anatomy, \mathcal{F} is the Fourier operator, $M \in \mathbb{R}^N$ is a binary undersampling mask, \circ is element-wise multiplication and n is an additive noise. For the sake of simplicity, we assume $n \sim \mathcal{N}(0, \sigma^2)$ [16].

Direct reconstruction of the MRI image x from the undersampled data is an ill-posed inverse problem that cannot be simply solved using linear approaches. Naïve reconstruction by zero-filling of the missing k-space data and application of the IFT will result in aliased image which is clinically meaningless [2].

The non-linear CS approach enables high-quality reconstruction from the undersampled k-space by imposing a sparsity constraint, Ψ to regularize the ill-posed inverse problem. The reconstructed image, \hat{x} , is obtained by solving the following constrained optimization problem:

$$\hat{x} = \arg \min_x \|M \circ \mathcal{F}(x) - k_{us}\|_2 + \lambda \Psi(x) \quad (2)$$

where λ is the regularization weight balancing between the data term and the assumed prior. Examples to the sparsifying transform Ψ include the total-variation and the wavelet transforms [7]. Recently, Jalal et al. [12] suggested to replace the sparsifying transform Ψ with a DNN-based generative

prior. Various optimization techniques were developed to address the challenging CS optimization problem [17]. Yet, the high computational complexity and limited ability to overcome image quality degradation at high acceleration rates may interfere clinical utilization [17].

Recently, DNN-based methods were applied for MRI reconstruction from undersampled data either on the image domain or on the k-space domain. In the k-space domain, the goal of these methods is to predict the fully sampled k-space data from the given undersampled k-space data. Without loss of generality, the prediction task can be represented as:

$$\widehat{k_{full}} = F_{\theta}(k_{us}) \quad (3)$$

where F_{θ} denotes the network function and θ represents the DNN weights. Taking a supervised learning approach, the DNN weights θ are estimated by minimizing the loss between the full k-space data predicted by the DNN, $\widehat{k_{full}}$, from the undersampled data, k_{us} , to the corresponding ground truth fully sampled k-space data, k_{full} , as follows:

$$\hat{\theta} = \arg \min_{\theta} \sum_{i=0}^{n_{data}} \left\| F_{\theta} \left(k_{us}^{(i)} \right) - k_{full}^{(i)} \right\|_1 \quad (4)$$

However, unlike the classical CS approach (Eq. 2), such methods are known to be unstable against the presence of variations in the acquisition process and the anatomical distribution [11, 12].

A key observation is that while the CS approach (Eq. 2) explicitly encode the undersampling mask M as part of the system forward model, DNN-based approaches essentially ignore the undersampling mask during training and inference. Even though augmentation techniques suggest to use undersampled k-space data from different masks during training [13], or in a physically-motivated loss functions [6], yet the undersampling mask information is not explicitly encoded in the DNN architecture and leveraged during inference. This may result in DNN instability compared to the classical CS counterpart.

3 Methods

3.1 Physically-primed DNN for MRI reconstruction

Our main hypothesis is that by explicitly encoding the undersampling mask in the DNN architecture and leveraging this information during inference, the DNN will be more capable to accurately generalize the ill-posed inverse problem associated with MRI reconstruction from undersampled data. Thus, it will be more robust against variations in the acquisition process and anatomical distribution. We introduce a physically-primed, U-Net [18] based, DNN architecture operating on the k-space domain. We represent the complex-valued k-space data as a two channel input, corresponding to the real and imaginary parts. We encode the undersampling mask M by adding a 3rd input channel to the DNN. The prediction of the full k-space data from the undersampled k-space data is defined as:

$$\widehat{k_{full}} = F_{\theta}(k_{us}, M) \quad (5)$$

The DNN weights θ are estimated by minimizing the loss between the full k-space data predicted by the DNN, $\widehat{k_{full}}$, from the undersampled data, k_{us} and the undersampling mask M , to the corresponding ground truth fully sampled k-space data, k_{full} , as follows:

$$\hat{\theta} = \arg \min_{\theta} \sum_{i=0}^{n_{data}} \left\| F_{\theta} \left(k_{us}^{(i)}, M^{(i)} \right) - k_{full}^{(i)} \right\|_1 \quad (6)$$

We encourage our physically-primed DNN model to generalize the ill-posed inverse problem of MRI reconstruction from undersampled k-space data by varying the undersampling mask M during training. Fig. 2 illustrates our physically-primed approach for training.

3.2 Implementation details

Our models are based on the suggested fastMRI U-Net [2], while modifying the output to be the summation of the k-space input and the network output. This network consists of two deep

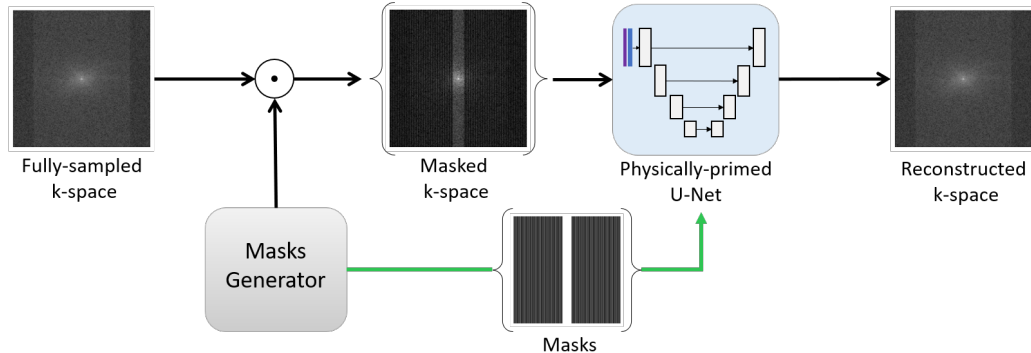


Figure 2: The fully sampled k-space is multiplied by a binary mask to create the undersampled k-space. Then the undersampled k-space (blue line) is fed into the physically primed DNN model along with the mask (purple line) used for the sampling.

convolutional networks, an encoder followed by a decoder. The encoder consists of blocks of two 3×3 convolutions, each followed by Rectified Linear Unit (ReLU) activation functions. The input to the encoder is a 3-channel data representing the concatenation of the complex k-space data (2-channels) and the binary undersampling mask (1-channel). The output of each block is down-sampled using a max-pooling layer with stride 2. The decoder consists of blocks with a similar structure to the encoder, where the output of each block is up-sampled using a bilinear up-sampling layer. The decoder concatenates the two inputs, the up-sampled output of the previous block and the output of the encoder block with the same resolution, to the first convolution in each block. At the end of the encoder there are two 1×1 convolutions that reduce the number of channels to two channels, representing the real and imaginary parts of the k-space data.

4 Experiments

4.1 Dataset

We used the publicly available fastMRI dataset [2], consisting of raw k-space data of knee and brain volumes. The knee images used in this study were directly obtained from the single coil track of the fastMRI dataset, while the brain images were reconstructed from fully sampled, multi-coil k-space data. Brain images were reconstructed by applying IFT to each individual coil and combining coils images with geometric averaging. The training set consisted of 34742 knee slices. We split the fastMRI knee validation set into validation and test sets since the original fastMRI test set does not allow applying random undersampling. The splitting ratio was 2:1, yielding 5054 slices for validation and 2081 slices for test. Brain images (1000 slices) were used for test purposes only.

To further evaluate the clinical impact of our approach, we also used the bounding box annotations generated by subspecialist experts on the fastMRI knee and brain dataset provided by the fastMRI+ dataset [19]. Each bounding box annotation includes its coordinates and the relevant label for a given pathology on a slice-by-slice level. Pathology annotations were marked in 39% of our training set, 28% of the validation set, and 51% of the test set. These annotations enabled us to examine the clinical relevance of our models performance on pathological regions.

4.2 Undersampling masks

We retrospectively undersampled the fully sampled k-space data by element-wise multiplication with randomly generated binary masks. The acceleration factor (R) was set to four or eight, where the undersampled k-space included 8% or 4% of the central region, respectively. The remaining k-space lines were sampled in three different ways to achieve the desired acceleration factor. The first sampling pattern was an equispaced mask with a fixed offset, meaning that the remaining k-space lines were sampled with equal spacing. The second sampling pattern was an equispaced mask with a varying offset, meaning that the remaining k-space lines were sampled with equal spacing but with random offset from the start. The third sampling pattern was a random mask, meaning that

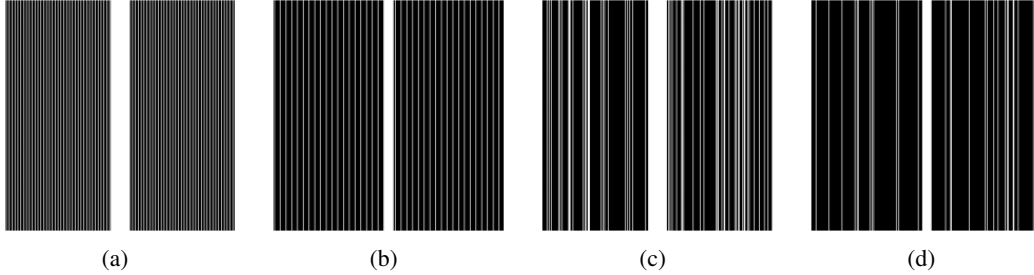


Figure 3: Masks patterns. (a) equispaced mask with $R=4$, (b) equispaced mask with $R=8$, (c) random mask with $R=4$, and; (d) random mask with $R=8$.

the remaining k -space lines were uniformly sampled. Fig. 3 depicts representative examples of the undersampling masks.

4.3 Training settings

We trained three models on the undersampled k -space with $R=4$. The undersampling pattern of the first model was fixed equispaced (Fixed). The undersampling pattern of the two other models was varying equispaced, while the input of one of them is the two-channel k -space (Baseline), and the input of the second one consists of three channels where the third channel is the mask pattern (Mask). We trained the models on transformed k -space to account for the orders of magnitude difference between the DC coefficient and the rest of the coefficients in the k -space. Specifically we used the following transformation:

$$k_t = \log(k + 1) \cdot 10^5 \quad (7)$$

All models were trained using the RMSprop algorithm. The initial learning rates were optimized for each model. An initial learning rate of 0.01 was used for all models. The initial learning rate was multiplied by 0.1 after 40 epochs for all models. We used the L1 norm between the 2 channels fully sampled k -space and the 2 channels reconstructed k -space as the loss function. We trained our models on two Nvidia A100 GPUs, each for 200 epochs. Training time took about 48 hours for each model. We selected the models with the best validation loss for our experiments.

4.4 Experimental methodology

We examined the generalization capability of the networks by testing their performance with varying acquisition conditions and anatomical distributions. Specifically, we evaluated reconstruction performance for: 1) undersampling patterns (equispaced for training and random for test) different from those used during training, but a similar acceleration factor ($R=4$), 2) different acceleration factor ($R=4$ for training and $R=8$ for test), and; 3) different anatomical distribution (knee for training and brain for test).

We used standard evaluation metrics, including the average normalized mean square error (NMSE), Peak Signal-to-Noise Ratio (PSNR) and Structural Similarity (SSIM) to assess the different models performance. To specifically determine the clinical relevance of our approach, we calculated performance metrics separately for the entire images and for clinically relevant regions that include pathologies. We used the clinical regions annotations from the fastMRI+ dataset [19]. We determined statistically significant differences between our approach and a baseline model trained with undersampling mask data augmentation with a paired Student’s t -test.

4.5 Results

Fig. 4 presents representative reconstruction results in cases of similar anatomical distribution and variation in the acquisition process, i.e. knee images with $R=4$ and different sampling masks in test. Fig. 5 presents representative reconstruction results in cases of variation in the anatomical distribution, i.e. brain images in test.

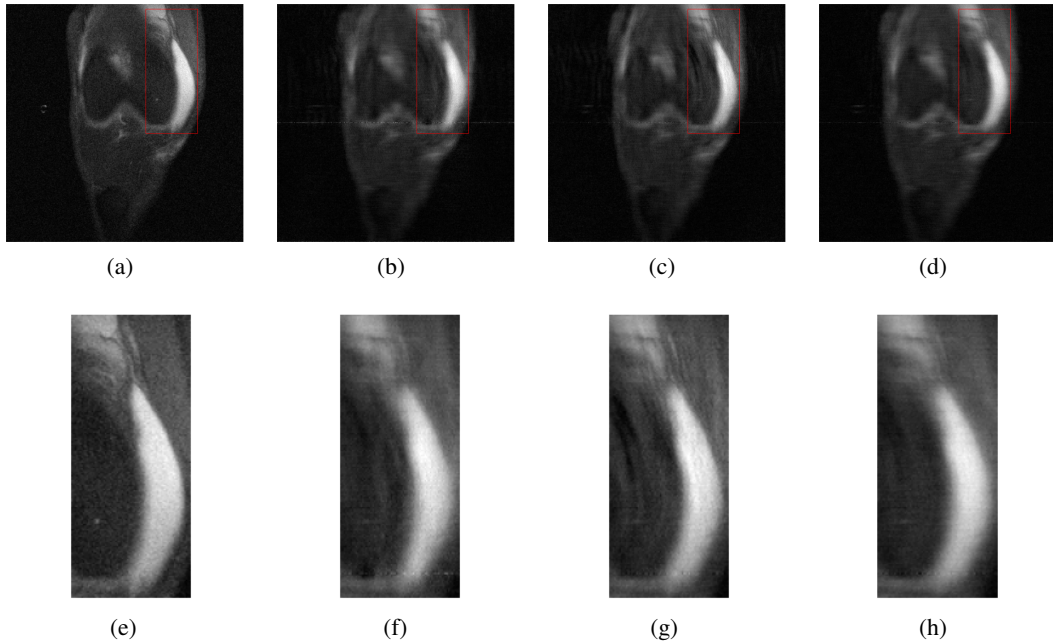


Figure 4: Reconstructed images along with zoom-in clinical annotation (red bounding box) for variation in the acquisition process, i.e., knee data undersampled with a random mask and $R=4$ in test. (a/e) target image, (b/f) reconstruction of fixed model (PSNR=28.87/25.47, SSIM=0.6043/0.6524), (c/g) reconstruction of baseline model (PSNR=29.12/25.98, SSIM=0.60122/0.663), and; (d/h) reconstruction of mask model (PSNR=29.58/26.66, SSIM=0.6325/0.7026).

Table 1: Entire image reconstruction accuracy for varying equispaced mask patterns in test.

R test	Model	NMSE	PSNR	SSIM
4	Fixed	0.05064 +/- 0.05197	30.08 +/- 5.48	0.6783 +/- 0.217
	Baseline	0.04211 +/- 0.05201	31.18 +/- 6.422	0.704 +/- 0.2176
	Mask	0.04197 +/- 0.05204	31.2 +/- 6.438	0.7043 +/- 0.2177
8	Fixed	0.08887 +/- 0.06282	27.33 +/- 4.645	0.5604 +/- 0.262
	Baseline	0.08003 +/- 0.05827	27.8 +/- 4.706	0.5767 +/- 0.2476
	Mask	0.07905 +/- 0.05736	27.85 +/- 4.721	0.5805 +/- 0.2461

Tables 1 and 2 summarize model performance on the entire image and for the clinically relevant regions, respectively, for the same anatomical distribution (i.e knee data) but with variations in the acquisition process (i.e. different equispaced sampling mask). Similarly, Tables 3 and 4 summarize model performance for random sampling masks in test. In all cases, the physically-primed model (Mask) has significantly better reconstruction accuracy (Paired student’s t-test, $p \ll 0.01$). The improved accuracy indicates a better generalization and robustness against variations in the acquisition process compared to models trained with and without mask augmentation. It is important to note that the improved performance is evident mostly in the clinically-relevant regions which are critical for clinical diagnosis.

Tables 5 and 6 demonstrate the generalization capacity of our physically-primed model in case of variation in the anatomical distribution, i.e. training on knee data while testing on brain data for the entire image and for the clinically-relevant regions, respectively. Our physically-primed model (mask) performed significantly better (Paired student’s t-test, $p \ll 0.01$) than the models trained with and without mask augmentation.

The improved robustness of our physically-primed model against variations in both the acquisition process and the anatomical distribution, suggest better generalization capacity beyond more common data augmentation techniques.

Table 2: Pathological regions reconstruction accuracy for varying equispaced mask patterns in test.

R test	Model	NMSE	PSNR	SSIM
4	Fixed	0.06059 +/- 0.09013	20.36 +/- 5.133	0.6374 +/- 0.266
	Baseline	0.05073 +/- 0.07628	21.22 +/- 5.332	0.6797 +/- 0.2415
	Mask	0.05013 +/- 0.07356	21.26 +/- 5.327	0.6807 +/- 0.2408
8	Fixed	0.1324 +/- 0.3375	17.07 +/- 4.649	0.4268 +/- 0.3105
	Baseline	0.1223 +/- 0.2854	17.44 +/- 4.755	0.4528 +/- 0.3083
	Mask	0.1193 +/- 0.3246	17.59 +/- 4.659	0.4638 +/- 0.3014

Table 3: Entire image reconstruction accuracy for random mask in test.

R test	Model	NMSE	PSNR	SSIM
4	Fixed	0.05759 +/- 0.05625	29.47 +/- 5.453	0.6374 +/- 0.2411
	Baseline	0.05187 +/- 0.05623	30.08 +/- 5.931	0.6519 +/- 0.239
	Mask	0.05013 +/- 0.05547	30.23 +/- 5.955	0.6592 +/- 0.2357
8	Fixed	0.09473 +/- 0.06802	27.07 +/- 4.672	0.5403 +/- 0.2815
	Baseline	0.08718 +/- 0.06259	27.42 +/- 4.636	0.552 +/- 0.2674
	Mask	0.08557 +/- 0.06079	27.49 +/- 4.665	0.5549 +/- 0.2597

Table 4: Pathological regions reconstruction accuracy for random mask in test.

R test	Model	NMSE	PSNR	SSIM
4	Fixed	0.07082 +/- 0.1018	19.62 +/- 4.839	0.5815 +/- 0.2899
	Baseline	0.06401 +/- 0.09236	20.12 +/- 5.008	0.6091 +/- 0.281
	Mask	0.05946 +/- 0.0852	20.43 +/- 4.973	0.6206 +/- 0.2713
8	Fixed	0.1377 +/- 0.2631	16.77 +/- 4.577	0.391 +/- 0.3098
	Baseline	0.1311 +/- 0.2524	17.06 +/- 4.713	0.4096 +/- 0.3123
	Mask	0.1228 +/- 0.2367	17.31 +/- 4.644	0.429 +/- 0.3048

Table 5: Entire image reconstruction accuracy on brain dataset for fixed equispaced mask in test.

R test	Model	NMSE	PSNR	SSIM
4	Fixed	0.182 +/- 0.3004	22.23 +/- 7.154	0.5093 +/- 0.2493
	Baseline	0.1147 +/- 0.1303	23.35 +/- 5.51	0.5455 +/- 0.1786
	Mask	0.02199 +/- 0.01034	29.92 +/- 4.55	0.7442 +/- 0.139
8	Fixed	0.1312 +/- 0.1226	22.48 +/- 5.041	0.412 +/- 0.2257
	Baseline	0.1053 +/- 0.129	23.53 +/- 4.57	0.4587 +/- 0.2068
	Mask	0.04726 +/- 0.0242	26.64 +/- 4.189	0.6628 +/- 0.1576

Table 6: Pathological regions reconstruction accuracy on brain dataset for fixed equispaced mask in test.

R test	Model	NMSE	PSNR	SSIM
4	Fixed	0.1542 +/- 0.7087	16.41 +/- 8.643	0.3731 +/- 0.4088
	Baseline	0.105 +/- 0.3544	17.65 +/- 7.585	0.4185 +/- 0.4031
	Mask	0.02502 +/- 0.06294	23.8 +/- 7.615	0.6421 +/- 0.2506
8	Fixed	0.105 +/- 0.235	16.87 +/- 6.588	0.294 +/- 0.356
	Baseline	0.09502 +/- 0.2554	17.68 +/- 7.031	0.3007 +/- 0.3833
	Mask	0.04952 +/- 0.1054	20.78 +/- 7.396	0.4544 +/- 0.2891

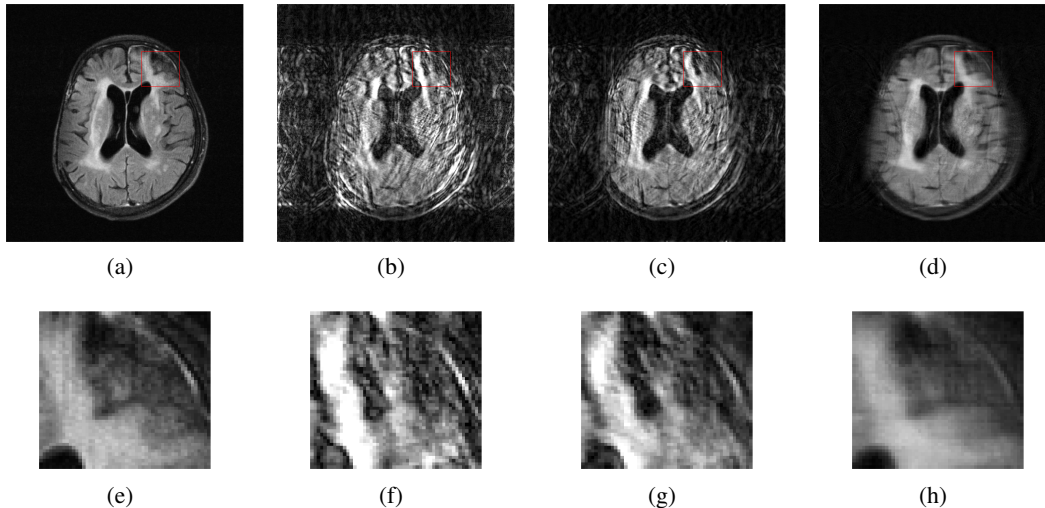


Figure 5: Reconstructed images along with zoom-in clinical annotation (red bounding box) for variation in the anatomical distribution (brain data on test) undersampled with equispaced mask and $R=4$ in test. (a/e) target image, (b/f) reconstruction of fixed model (PSNR=14.85/10.92, SSIM=0.2405/0.364), (c/g) reconstruction of baseline model (PSNR=20.17/15.53, SSIM=0.4315/0.5377), and; (d/h) reconstruction of mask model (PSNR=27.75/24.67, SSIM=0.7446/0.7779)

5 Discussion and Conclusion

We introduced a physically-primed DNN architecture to address the stability gap in deep-learning based MRI reconstruction from undersampled k-space data. The previously observed stability gap indicates limited generalization of the associated ill-posed inverse problem compared to classical methods. This stability gap practically impede DNN-based MRI reconstruction from undersampled data in the clinical setting. While previous approaches aimed to address the stability gap through data augmentation and physically motivated loss functions, our physically-primed DNN approach improves the generalization capacity by encoding the forward model, including the undersampling mask, in the network architecture and introducing an appropriate training scheme with samples generated with various undersampling masks. Our experiments showed that encoding the undersampling mask as part of the DNN architecture improves generalization capacity, especially in clinically relevant regions, compared to previously proposed data augmentation techniques in multiple scenarios including changing the undersampling mask, modifying the sampling factor, and applying the DNN to reconstruct images acquired from a different anatomical region.

Our study has several limitations. First, our analysis was performed on single-coil volumes. In addition, we tested our hypothesis with a specific baseline architecture and used only a specific method to encode the undersampling mask into the DNN architecture. We suspect our conclusions will hold in the more clinically relevant multi-coil settings and advanced DNN approaches, but this is to be confirmed by future work. Further, we used quantitative metrics such as the PSNR and SSIM to objectively assess the added value of our approach. However, the PSNR and SSIM may not capture the needs of real-world radiologists. A more detailed study is required before the proposed techniques can be clinically adopted. Finally, we used the publicly available fastMRI data which is limited to two anatomical regions and specific MR sequences. Thus, it may not represent the entire range of possible MRI scans. The impact of our approach should be evaluated on various MRI scans and sequences in future studies.

In conclusion, our physically-primed approach has the potential to improve the generalization capacity and robustness of DNN-based methods for MRI reconstruction from undersampled k-space data. Thus, in turn, our approach has the potential to facilitate the utilization of DNN-based MRI reconstruction methods in the clinical setting.

References

- [1] Z.-P. Liang and P. C. Lauterbur, *Principles of magnetic resonance imaging*. SPIE Optical Engineering Press Bellingham, 2000.
- [2] J. Zbontar, F. Knoll, A. Sriram, T. Murrell, Z. Huang, M. J. Muckley, A. Defazio, R. Stern, P. Johnson, M. Bruno *et al.*, “fastmri: An open dataset and benchmarks for accelerated mri,” *arXiv preprint arXiv:1811.08839*, 2018.
- [3] D. A. Feinberg, J. D. Hale, J. C. Watts, L. Kaufman, and A. Mark, “Halving mr imaging time by conjugation: demonstration at 3.5 kg.” *Radiology*, vol. 161, no. 2, pp. 527–531, 1986.
- [4] M. A. Griswold, P. M. Jakob, R. M. Heidemann, M. Nittka, V. Jellus, J. Wang, B. Kiefer, and A. Haase, “Generalized autocalibrating partially parallel acquisitions (grappa),” *Magnetic Resonance in Medicine: An Official Journal of the International Society for Magnetic Resonance in Medicine*, vol. 47, no. 6, pp. 1202–1210, 2002.
- [5] K. P. Pruessmann, M. Weiger, M. B. Scheidegger, and P. Boesiger, “Sense: sensitivity encoding for fast mri,” *Magnetic Resonance in Medicine: An Official Journal of the International Society for Magnetic Resonance in Medicine*, vol. 42, no. 5, pp. 952–962, 1999.
- [6] K. Hammernik, T. Küstner, B. Yaman, Z. Huang, D. Rueckert, F. Knoll, and M. Akçakaya, “Physics-driven deep learning for computational magnetic resonance imaging,” *arXiv preprint arXiv:2203.12215*, 2022.
- [7] M. Lustig, D. Donoho, and J. M. Pauly, “Sparse mri: The application of compressed sensing for rapid mr imaging,” *Magnetic Resonance in Medicine: An Official Journal of the International Society for Magnetic Resonance in Medicine*, vol. 58, no. 6, pp. 1182–1195, 2007.
- [8] Y. Chen, C.-B. Schönlieb, P. Liò, T. Leiner, P. L. Dragotti, G. Wang, D. Rueckert, D. Firmin, and G. Yang, “Ai-based reconstruction for fast mri—a systematic review and meta-analysis,” *Proceedings of the IEEE*, vol. 110, no. 2, pp. 224–245, 2022.
- [9] T. Eo, Y. Jun, T. Kim, J. Jang, H.-J. Lee, and D. Hwang, “Kiki-net: cross-domain convolutional neural networks for reconstructing undersampled magnetic resonance images,” *Magnetic resonance in medicine*, vol. 80, no. 5, pp. 2188–2201, 2018.
- [10] A. Sriram, J. Zbontar, T. Murrell, A. Defazio, C. L. Zitnick, N. Yakubova, F. Knoll, and P. Johnson, “End-to-end variational networks for accelerated mri reconstruction,” in *International Conference on Medical Image Computing and Computer-Assisted Intervention*. Springer, 2020, pp. 64–73.
- [11] V. Antun, F. Renna, C. Poon, B. Adcock, and A. C. Hansen, “On instabilities of deep learning in image reconstruction and the potential costs of ai,” *Proceedings of the National Academy of Sciences*, vol. 117, no. 48, pp. 30 088–30 095, 2020.
- [12] A. Jalal, M. Arvinte, G. Daras, E. Price, A. G. Dimakis, and J. Tamir, “Robust compressed sensing mri with deep generative priors,” *Advances in Neural Information Processing Systems*, vol. 34, pp. 14 938–14 954, 2021.
- [13] F. Liu, A. Samsonov, L. Chen, R. Kijowski, and L. Feng, “Santis: sampling-augmented neural network with incoherent structure for mr image reconstruction,” *Magnetic resonance in medicine*, vol. 82, no. 5, pp. 1890–1904, 2019.
- [14] C. M. Hyun, H. P. Kim, S. M. Lee, S. Lee, and J. K. Seo, “Deep learning for undersampled mri reconstruction,” *Physics in Medicine & Biology*, vol. 63, no. 13, p. 135007, 2018.
- [15] G. Yang, S. Yu, H. Dong, G. Slabaugh, P. L. Dragotti, X. Ye, F. Liu, S. Arridge, J. Keegan, Y. Guo *et al.*, “Dagan: deep de-aliasing generative adversarial networks for fast compressed sensing mri reconstruction,” *IEEE transactions on medical imaging*, vol. 37, no. 6, pp. 1310–1321, 2017.
- [16] S. Aja-Fernández and G. Vegas-Sánchez-Ferrero, “Statistical analysis of noise in mri,” *Switzerland: Springer International Publishing*, 2016.

- [17] J. C. Ye, "Compressed sensing mri: a review from signal processing perspective," *BMC Biomedical Engineering*, vol. 1, no. 1, pp. 1–17, 2019.
- [18] O. Ronneberger, P. Fischer, and T. Brox, "U-net: Convolutional networks for biomedical image segmentation," in *International Conference on Medical image computing and computer-assisted intervention*. Springer, 2015, pp. 234–241.
- [19] R. Zhao, B. Yaman, Y. Zhang, R. Stewart, A. Dixon, F. Knoll, Z. Huang, Y. W. Lui, M. S. Hansen, and M. P. Lungren, "fastmri+: Clinical pathology annotations for knee and brain fully sampled multi-coil mri data," *arXiv preprint arXiv:2109.03812*, 2021.